SANDIA REPORT
SAND2021-1150
Printed February 2021

Elucidating Hydrogen Reaction-Induced Water Desorption from Oxide-Passivated Metal Surfaces for Plasma Applications

Kyle Cochrane, Anastasia G. Ilgen, Ronald G. Goeke, Alex Wilson, and Kevin Leung

Prepared by
Sandia National Laboratories
Albuquerque, New Mexico
87185 and Livermore,
California 94550

Issued by Sandia National Laboratories, operated for the United States Department of Energy by National Technology & Engineering Solutions of Sandia, LLC.

NOTICE: This report was prepared as an account of work sponsored by an agency of the United States Government. Neither the United States Government, nor any agency thereof, nor any of their employees, nor any of their contractors, subcontractors, or their employees, make any warranty, express or implied, or assume any legal liability or responsibility for the accuracy, completeness, or usefulness of any information, apparatus, product, or process disclosed, or represent that its use would not infringe privately owned rights. Reference herein to any specific commercial product, process, or service by trade name, trademark, manufacturer, or otherwise, does not necessarily constitute or imply its endorsement, recommendation, or favoring by the United States Government, any agency thereof, or any of their contractors or subcontractors. The views and opinions expressed herein do not necessarily state or reflect those of the United States Government, any agency thereof, or any of their contractors.

Printed in the United States of America. This report has been reproduced directly from the best available copy.

Available to DOE and DOE contractors from
U.S. Department of Energy
Office of Scientific and Technical Information
P.O. Box 62
Oak Ridge, TN 37831

Telephone: (865) 576-8401
Facsimile: (865) 576-5728
E-Mail: reports@osti.gov
Online ordering: http://www.osti.gov/scitech

Available to the public from
U.S. Department of Commerce
National Technical Information Service
5301 Shawnee Rd
Alexandria, VA 22312

Telephone: (800) 553-6847
Facsimile: (703) 605-6900
E-Mail: orders@ntis.gov
Online order: https://classic.ntis.gov/help/order-methods/

ABSTRACT

Elucidating the mechanisms responsible for sub-microsecond desorption of water and other impurities from electrode surfaces at high heating rates is crucial for understanding pulsed power behavior. Ionization of desorbed impurities in the vacuum regions causes power or current loss; devising methods to limit such desorption during the short time scale of pulsed power is needed to improve corresponding applications. Previous molecular modeling studies have strongly suggested that, under high vacuum conditions, the amount of water impurity desorbing from oxide surfaces on metal electrodes is at a sub-monolayer level at room temperature, which appears insufficient to explain observed pulsed power energy losses at high current densities. In this work, we apply Density Functional Theory (DFT) techniques to show that hydrogen trapped inside iron metal can diffuse into hematite (α-Fe_2O_3) on the metal surface, ultimately reacting with the oxide to form Fe(II) and H_2O. The latter desorbs at elevated temperature and may explain the anomalous amount of desorbed impurity inferred from pulsed-power experiments. We also apply a suite of characterization techniques to demonstrate that when iron metal is heated to 650 ^{o}C, the dominant surface oxide component becomes α-Fe_2O_3. The oxide facets exposed are found to be a mixture of (0001), (10-10), and others, in agreement with the DFT models used.

ACKNOWLEDGEMENTS

Ronald Goeke first suggested the hydrogen reaction generation of water mechanism which is the focus of this report, based on work he and Sean Simpson performed. We thank Alan Wright for calculations of hydrogen binding calculations, Mark Rodriguez for X-ray Diffraction results, Sara Dickens and Luis Jauregui for EBSD, Jacquilyn Weeks for editing, Louise Criscenti for her insights into stainless steel, and Sean Simpson for useful discussions. This project was supported by Sandia Laboratory Directed Research and Development (LDRD) project 209240. Sandia National Laboratories is a multimission laboratory managed and operated by National Technology and Engineering Solutions of Sandia, LLC, a wholly owned subsidiary of Honeywell International, Inc., for the U.S. Department of Energy's National Nuclear Security Administration under contract DE-NA0003525. This paper describes objective technical results and analysis. Any subjective views or opinions that might be expressed in the paper do not necessarily represent the views of the U.S. Department of Energy or the United States Government.

CONTENTS

1. Introduction 6
2. Methods 9
3. Results 10
4. Conclusions 18

LIST OF FIGURES

Figure 1. Raman Spectrum of Oxidized Fe(0) Sample 10
Figure 2. Raw and Oxidized Fe(0) Sample 11
Figure 3. 3-D Map and Depth Profile of Fe(0) Sample 11
Figure 4. Raman Map of Fe(0) Sample 12
Figure 5. Raman Spectra during Heating and Oxidation of Fe(0) Sample 13
Figure 6. EBSD IPF-Z for a Fe_2O_3 Coupon and Legend 14
Figure 7. Grazing Angle X-Ray Diffraction Analysis 15
Figure 8. DFT and Temkin-like Predictions for Water Desorption from Fe_2O_3 (10-10) Surface 16

LIST OF TABLES

Table 1. Raman Frequencies of Iron Oxide Coating 10

1. INTRODUCTION

The interactions between water and metal oxide surfaces are of interest to many fundamental science disciplines, including vacuum-related studies [1]. Iron oxides are of particular interest because they are the predominant phases found on steel surfaces. Their formation and interaction with water are relevant to corrosion, and steel corrosion is a multitrillion-dollar problem [2]. While corrosion due to atmospheric water is a known concern and is the subject of extensive studies, rapid release of water vapor and hydrogen from oxide surfaces under vacuum (~10^{-5} torr vapor pressure) common to many pulsed power applications is not completely understood. It has been inferred that up to tens of monolayers (ML) worth of hydrogen- and/or carbon-containing impurities desorb from the surface in vacuum [3], especially during pulsed operations when the electrodes carry large currents that heat up the electrodes in sub-microsecond time scales [4,5]. These impurities bridge the anode/cathode gap causing undesirable current losses. The origin of the large amounts of impurity has not been explained in a vacuum setting at molecular length-scales.

Take the low energy (0001) facet of α-Fe_2O_3 as an example. A sub-ML of molecular or dissociated water molecules is known to exist on the low energy (0001) facet of α-Fe_2O_3 at room temperature [6]. Computationally, molecular and dissociated H_2O have been predicted to be almost isoenergetic, and the barrier for interconversion is small on this facet [7,8]. This has allowed us to approximate water as non-dissociated molecules. With this approach, we have used molecular simulations to show that, if > 0.4 ML of water initially exists on the surface at 10^{-5} torr, desorption rapidly occurs at room temperature before heating occurs [9,10], in qualitative agreement with measurements [6]. Therefore, these surfaces do not support multi-layers of adsorbed water under low pressure. On polycrystalline oxide surfaces, other facets like (10-10) are also exposed [11,12]. Previous studies have predicted that these higher energy surfaces cause partial dissociation of adsorbed water molecules, again at sub-ML coverage [12].

The situation is different in naturally occurring systems, where iron oxide surfaces are fully hydroxylated. For example, iron oxyhydroxides (FeOOH) occur naturally in aqueous geochemical systems, and they contain a macroscopic number of proton-containing hydroxyl groups [13]. However, FeOOH is thermodynamically unstable under low-humidity conditions and unlikely to be present on surfaces that have not been immersed in water, such as those being examined experimentally here. These observations strongly suggest that the amount of "H_2O" content on metal oxide surfaces not immersed in water should be limited to sub-ML quantities at 10^{-5} torr. So the puzzle remains regarding why excess quantities of water are frequently observed in pulsed power applications such as Sandia National Laboratories' Z-machine [4].

The above conclusion that < 1 ML exists on surfaces relevant to vacuum technologies was obtained using only crystalline oxide samples, or molecular models thereof. In particular, the presence of metals underneath the oxide, such as stainless steel or iron, has often been ignored in previous modeling work, and they may significantly affect surface properties. Here we propose a hypothesis that reconciles the sub-ML of water known to reside on oxide surfaces, and the multi-ML of water desorbing from steel electrodes under vacuum. The proposed mechanism is based on the well-known fact that a finite concentration of hydrogen resides in iron and steel[15], as it does in many metals[16]. We hypothesize that these hydrogen atoms residing in crystalline metal

regions can diffuse into the surface oxide, especially at elevated temperature. Once hydrogen reaches the oxide surface, it reacts with hydroxyl group to form and release water.

Since the proposed release of water molecules partly come from oxygen anions that are in the oxide framework, these molecules are more strongly bound to the surface than adsorbed water dosed on the surface. Therefore, one expects higher water binding energies and slower desorption rates. Whether H_2O released *via* this pathway is commensurate with vacuum technology conditions needs to be investigated. In this work, we apply Density Functional Theory (DFT) calculations to examine the energetics of this reaction inside hematite (α-Fe_2O_3) and on some of its surface facets. We demonstrate that H + oxide -> H_2O is indeed feasible in pulsed-power time and temperature scales. Electrochemical reduction of some Fe(III) ions to Fe(II) must concomitantly occur if H atoms reacts with the oxide. In that sense, our modeling work is closely related to H_2O adsorbed on oxide surfaces in oxygen vacancies which creates Fe(II) [14]; however, instead of placing a water molecule on a given surface, we place one or more hydrogen atoms and/or hydrogen dimers on the surface and examine the desorption energetics.

To support the models adopted in DFT calculations, we performed several experiments. First, we demonstrate that α-Fe_2O_3 is, indeed, present on iron metal surfaces. Oxide films grown at room temperature are typically a few nanometers thick; although elemental analysis techniques like X-ray photoelectron spectroscopy (XPS) are illuminating, the oxide crystal structures are difficult to characterize because of the small grain sizes. Using standard surface characterization techniques on oxide-coated metal surfaces, the oxide phase, its crystallinity, and the exposed oxide facets are difficult to elucidate. While scanning tunneling microscopy with atomic resolution has been applied to observe nano-crystallites of oxides on steel surfaces [17], such high-resolution experimental methods require special sample preparation and have not been applied to pure iron. In this work, we circumvent the spatial resolution problems by heating iron samples in air at 650 ^{o}C [18, 19], to create oxide grains large enough to analyze using Raman spectroscopy and electron backscatter diffraction (EBSD) analysis. Our synthesis and characterization work justify the oxide phase used in the DFT calculations for these specially prepared samples. We propose that this heating procedure should be used as future experimental platforms for temperature programmed desorption (TPD) measurements on both iron and steel samples, so that water desorption measurements will be performed on well-characterized surfaces and can be quantitatively compared to our predictions.

This work uses iron as a surrogate for austenitic steel used in many pulsed-power applications. It is useful to discuss the relation between body center cubic (BCC) iron, and the dominant iron domain in austenitic steel which has a face center cubic (FCC) lattice structure. For the purpose of our hypothesis, the only difference is the hydrogen binding energy inside metallic iron regions. Both iron phases will be calculated in this work. Indeed, hydrogen embrittlement of steel is a technologically relevant research area.

Steel surface is passivated by a multi-crystalline film consisting of iron oxides, chromium oxides, and the oxides of other minority metal components; spinels with more than one transition metal ion are also known to exist [20, 21]. However, the outer regions of the surface oxide are expected to be dominated by α-Fe_2O_3 [22,23]. Regarding other oxide phases, hydrogen permeation and diffusion in α-Cr_2O_3 and α-Al_2O_3, isostructural to α-Fe_2O_3, have been the subjects of many DFT

studies [24-27]. Insertion of hydrogen atoms inside these oxides are less energetically favorable than Fe_2O_3 because Cr(II) and Al(II) formation are more electrochemically negative. Alumina has been proposed as a hydrogen blocking layer for nuclear energy applications [25]. The role of these oxide films on plasma applications can be investigated using methods similar to those discussed in this report.

2. METHOD

An iron coupon 99.5% Fe, obtained from Goodfellow Corporation was characterized using Raman spectroscopy and white light profilometry, then an oxide layer was formed on the surface during sample heating to 650 °C for 20 minutes. After cooling, the sample was sealed in a plastic bag, awaiting analysis. The sample, which now included an oxide layer, was again examined using Raman spectroscopy.

The post-oxidation Raman spectrum was collected using an XploRA Plus Raman microscope (HORIBA Scientific) with a cooled CCD detector (Jobin Yvon's Synapse camera). A laser with a 532 nm emission wavelength was used for excitation (radiation power ~100 mW at 10% to 25% power). An objective with 10x magnification and a numerical aperture of 0.25 was used for excitation, with a resulting laser spot diameter of 2.6 microns. Each spectrum was collected with 1 second exposure and averaged over 60 scans from 100 to 2000 cm^{-1}. Raman spectrometer calibration was performed every 24 hours using a polished silicon wafer. White light profilometry investigation was performed using Keyence VHX digital microscope.

Spatially resolved characterization of the crystal orientation surface was performed with a scanning electron microscope (SEM) using electron backscatter diffraction (EBSD) mapping. A polished iron coupon identical to the one used for Raman spectroscopy, was again heated in air to 650 °C for 20 min, for the purpose of growing an oxide layer thick enough for crystallographic characterization. Grazing angle X-ray Diffraction was used on this sample for phase identification.

We calculated energies associated with oxides using the density functional theory code VASP (Vienna *ab initio* Simulation Package) [28-34]. We used the general gradient approximation (GGA) with the exchange correlation functional Perdew, Burke, and Ernzerhof (PBE) [35].The pseudopotentials for iron, oxygen, and hydrogen were of the valence configuration d7s1, s2p4, and s1 respectively and the energy cutoff was 400 eV. Various Monkhorst k-point meshes were used [35]. Because of the strongly correlated 3d shell, we used the +U formulation [37-39] with a U-J of 4.5 eV. The smearing was Fermi-like with width 0.03 eV. The iron atoms were divided into two groups given an initial polarization guess of +4 or -4. Collinear spin polarization was used. The convergence criterion for the self-consistent electronic iterations was 1.0^{-4} eV. The hydroxylated (10-10) simulation cell adopt a 10.22x13.86x27 $Angstrom^3$ simulation cell. The base stoichiometry is $Fe_{56}O_{100}H_{32}$ prior to adding more H atoms.

The water desorption energy (ΔE_{desorb}) from a given configuration was calculated using

$$\Delta E_{desorb} = E(slab + H_2O) - E(slab) - E(H_2O),$$

where "slab" is the Fe_2O_3 solid simulation cell without the extra H_2O. We assume that ΔE_{desorb} is the same as the desorption activation energy (or barrier, ΔE^*) because, for molecular adsorbed H_2O, the two quantities are generally identical [10].

Binding energies of hydrogen atoms in FCC Fe were calculated using a 108-atom FCC Fe metal simulation cell, using spin-polarized DFT, the PBE functional, 7x7x7 Brillouin zone sampling, and a 268 eV energy cutoff. In BCC Fe, this was conducted using a 240-atom cell with 2x2x2 k-point sampling at the same energy cutoff.

3. RESULTS

3.1 Raman and Optical Spectroscopy

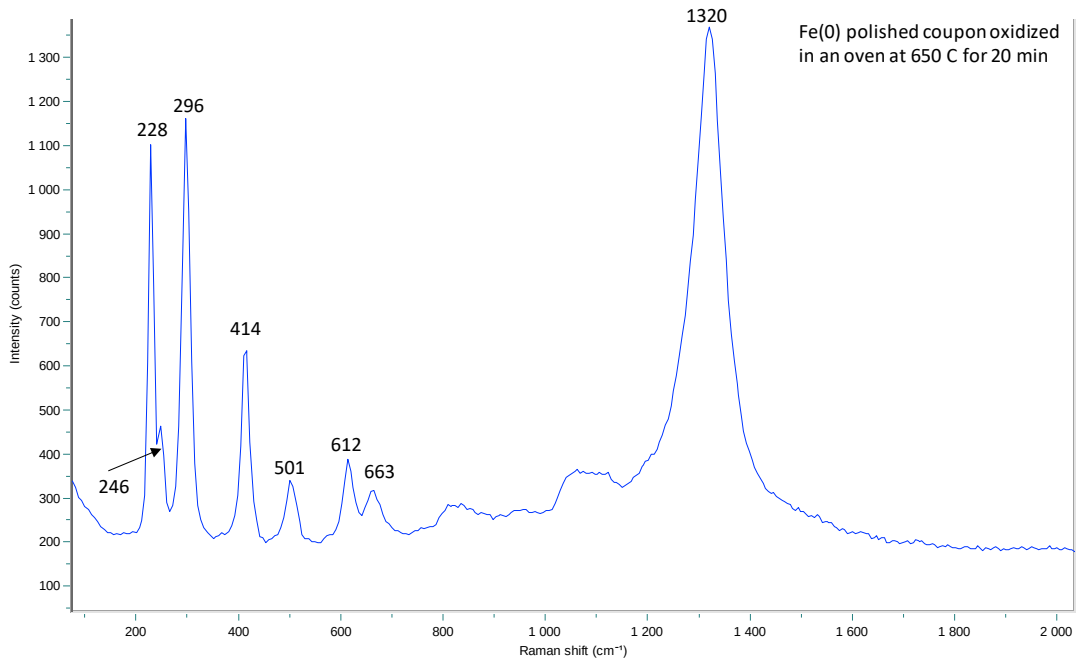

Figure 1. Raman spectrum of oxidized Fe(0) sample. Sample was oxidized at 650 °C in an oven for 20 minutes.

Raman spectrum of the oxidized coupon is shown in **Figure 1**. The observed bands and band assignments are shown in **Table 1**. These features agree with the report by Maslar et al., 2000 [40], where iron metal samples were analyzed using 647 nm and 785 nm lasers. The assignment of Raman band modes is made based on the recent publication for hematite (α-Fe_2O_3) single crystals by Marshall et al. (2020) [41].

Table 1. Raman frequencies (cm^{-1}) of iron oxide coating on the Fe(0) coupon measured in this work with 532 nm laser excitation at room temperature. Band mode assignment is based on theMarshall et al., 2020 study of single crystal hematite (α-Fe_2O_3) [41].

Peak position (cm^{-1})	Assignment		Peak position (cm^{-1})	Assignment	
	Mode	Phase		Mode	Phase
228	A_{1g}	α-Fe_2O_3	612	E_g	α-Fe_2O_3
296	E_g	α-Fe_2O_3	663	1LO	α-Fe_2O_3
414	E_g	α-Fe_2O_3	1320	2LO	α-Fe_2O_3
501	A_{1g}	α-Fe_2O_3			

The recorded optical images of polished and oxidized Fe(0) coupons are shown in **Figure 2**. The initial sample has minimal roughness (nm-scale) with small pits and lines which are likely polishing artifacts, while the oxidized sample has roughness at the 1 μm scale and irregular surface morphology (**Figure 2**).

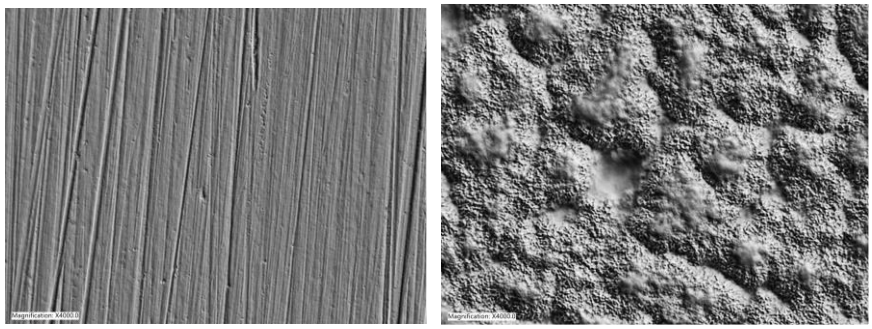

Figure 2. (a) Raw Fe(0) sample surface, magnification 4000; (b) Oxidized surface, magnification 4000.

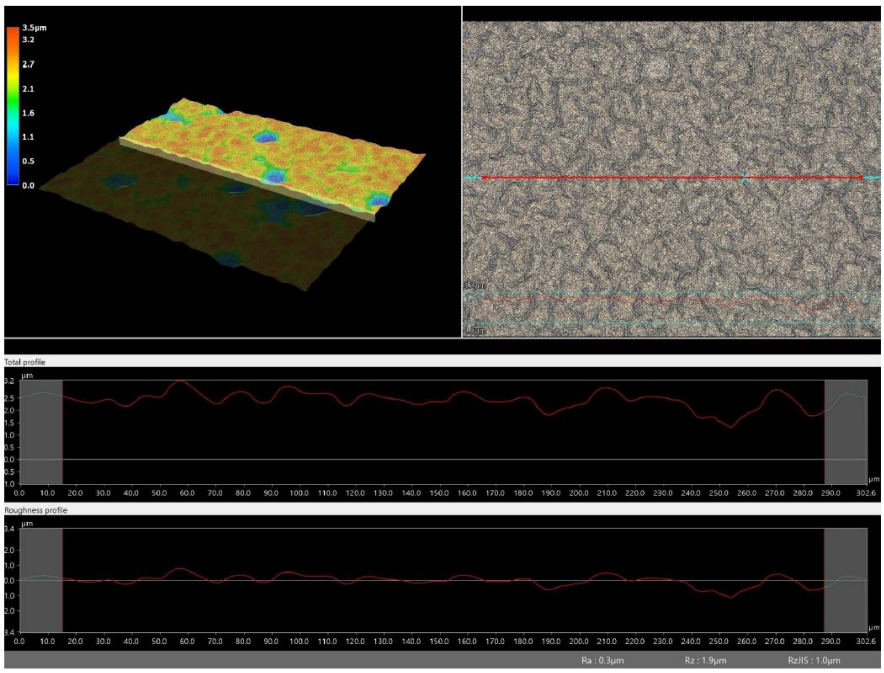

Figure 3. 3D map of the oxidized sample and corresponding depth profile. The surface morphology of the oxidized sample appears irregular, with "pits" throughout. There are no remnants of lines which were visible on the raw sample. The average roughness of the oxidized sample is ~1 µm.

Under an optical microscope, the sample surface appears inhomogeneous, which is in agreement with the white light profilometry measurements. To characterize potential spatial variability in the oxidized layer structure, we performed Raman mapping (**Figure 4**). Three "principal spectral components" were chosen to construct the composite map with three fundamental vibrational modes of hematite (α-Fe_2O_3): 228 cm^{-1} (A_{1g}), 414 cm^{-1} (E_g), and 1320 cm^{-1} (2LO). There is no conclusive Raman evidence of other Fe_2O_3 phases present. However, the surface roughness leads to different surface facets being exposed, thereby requiring an expanded scope for the DFT simulations, which now must examine more than one surface type.

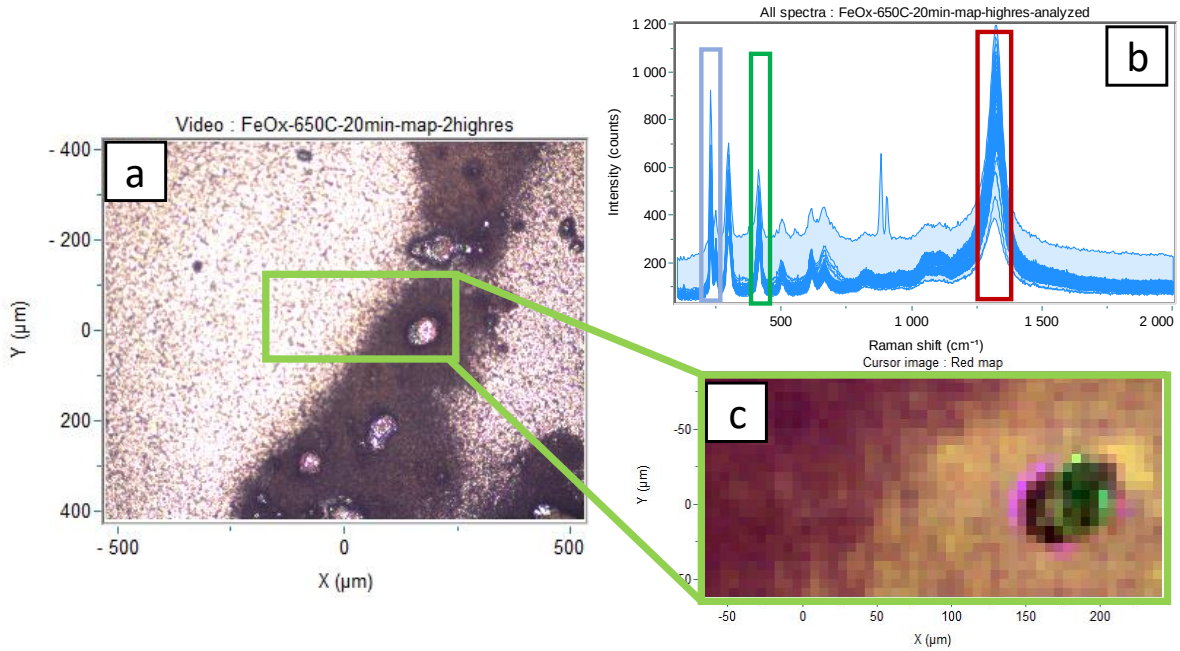

Figure 4. Raman map of the oxidized Fe(0) coupon; (a) optical image of the surface with highlighted area that was used for the Raman map; (b) Raman spectra collected from the highlighted area; three selected channels centered at 228 cm^{-1} (A_{1g}), 414 cm^{-1} (E_g), and 1320 cm^{-1} (2LO); (c) Raman map showing an overlap in intensities of the three selected channels.

3.2 In situ oxidation of iron metal sample

To characterize the time-dependent evolution of the α-Fe_2O_3 film growing on the iron metal surface, we placed a polished Fe(0) sample inside a Linkam THMS600 stage at room temperature and increased the temperature in 20-30 °C increments every 5 minutes to 530 °C, maintaining that temperature for the collection of Raman spectra using an XploRA Plus Raman microscope (HORIBA Scientific) with a cooled CCD detector (Jobin Yvon's Synapse camera). The resulting spectra are shown in **Figure 5** and show the onset of oxide film growth at 220 °C. We observed that the A_{1g}, E_g, and 1LO peaks in the freshly grown film are shifted to lower wavenumber values at the elevated temperature: 218 cm^{-1} (A_{1g}), 283 cm^{-1} (E_g), and 657 cm^{-1}(1LO). Potentially interesting dynamics in the development of Raman peaks: the peak at 657 cm^{-1} first appeared at 220 °C, then reached its maximum at 270 °C, and started decreasing in intensity with further increase in temperature. The peaks at 218 and 283 cm^{-1} started appearing at 250 °C and reached maximum intensity at the end of the heating cycle.

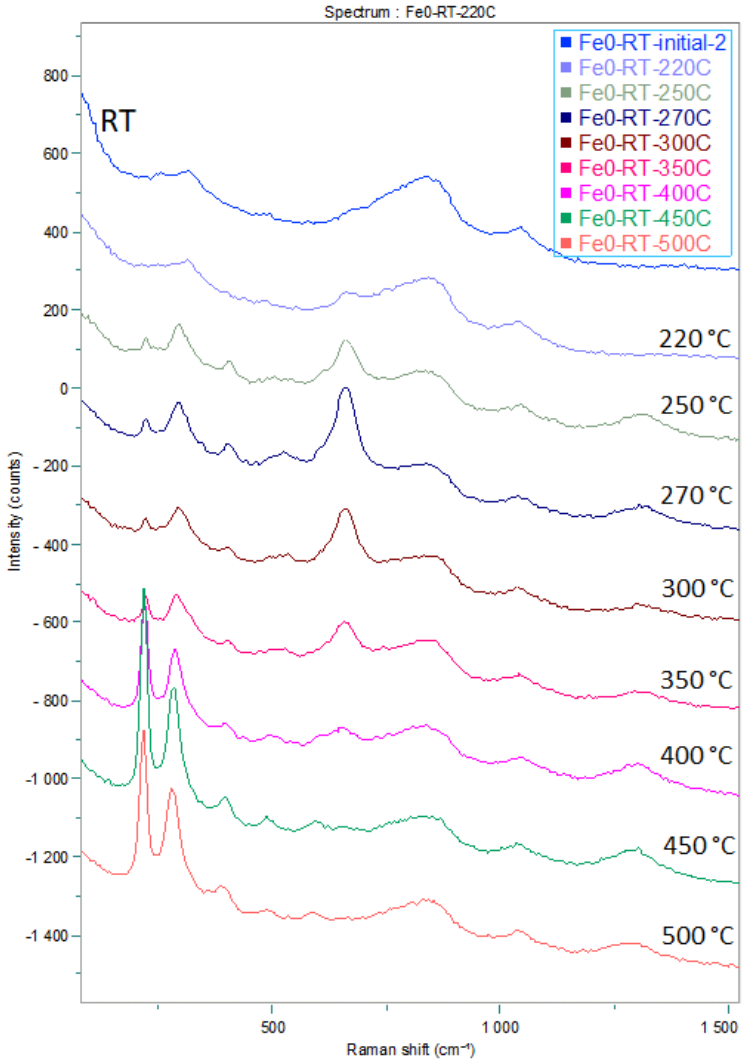

Figure 5. Raman spectra collected every 5 minutes during heating and oxidation of Fe(0) coupon.

3.3 Electron Backscatter Diffraction Analysis

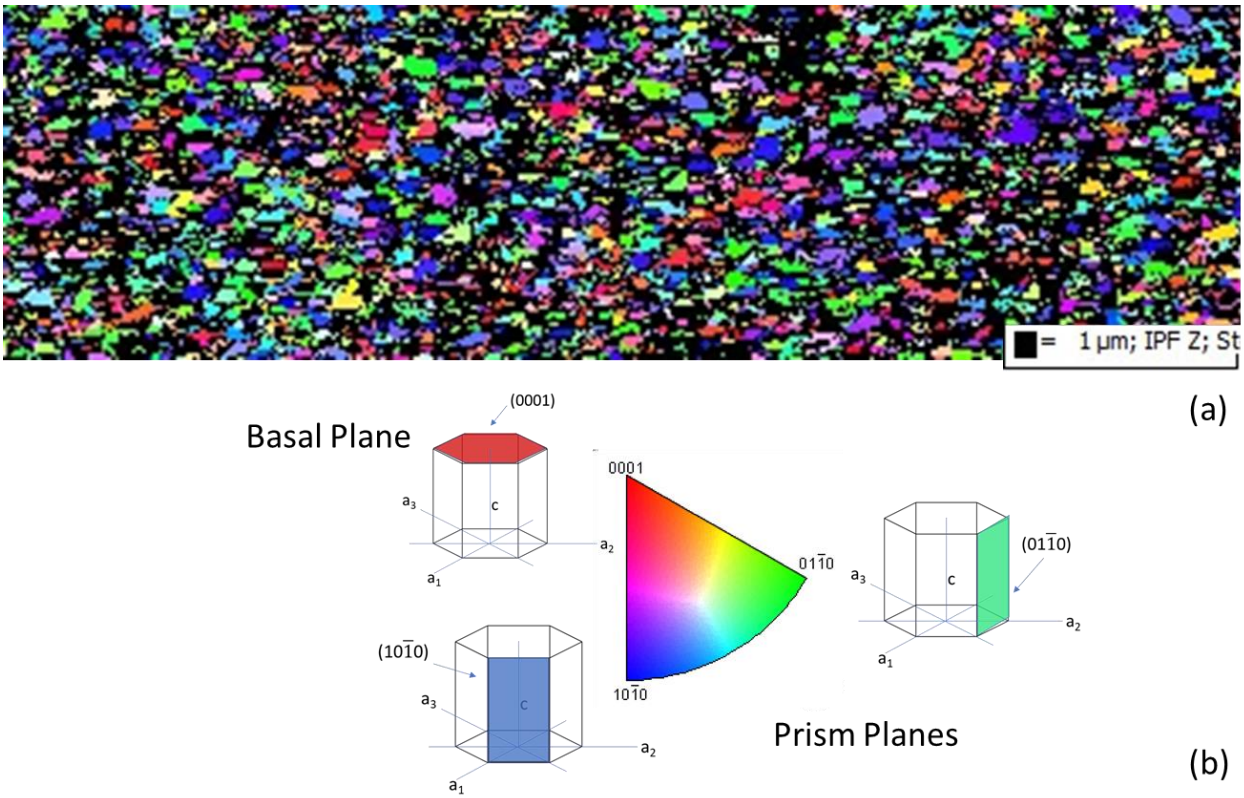

Figure 6. (a) EBSD IPF-Z for a Fe_2O_3 Coupon, (b) IPF legend for the EBSD map on this hexagonal crystal system

Fig. 6a depicts the EBSD results, showing the existence of (0001) and (10-10) facets on an α-Fe_2O_3 surface grown on iron samples at 650 ^oC. The top surface, as measured by EBSD, indexed to Fe_2O_3 hematite, confirming this as the outer oxide layer. The Inverse Pole Figure (IPF) color map in the Z-direction is shown in Figure . The dark areas are regions which were not indexed, most likely due to the small grain size. The larger grains observed by SEM on this sample were a few hundred nanometers in size. Both basal planes, shown in red and the prism planes seen in green and blue were observed oriented in the z-direction. We find no evidence of other iron oxide phases.

However, unlike the Raman analysis, Grazing Incidence X-Ray Diffraction (GI-XRD) (Fig. 7) confirmed the presence of both Fe_2O_3 hematite and a thicker Fe_3O_4 magnetite layer on the oxidized Fe coupon. There are at least two reasons for the apparent discrepancy. First, we note that the sample used for EBSD and X-ray analysis is distinct from those used for Raman studies (Figs. 1-5); the temperature was raised from room temperature to 650 ^oC at 10 ^oC/minute and held at 650 ^oC for at least 10 minutes. Second, the EBSD information depth is usually quoted as about 40 nm, while X-ray likely exhibits a larger penetration depth even in grazing incidence mode. We expect the more highly oxidized hematite phase to be closest to the surface (the most stable in oxygen environments), while Fe_3O_4 would be expected to form in more oxygen-deficient subsurface regions [22,23], and would be less important for the purpose of water desorption studies.

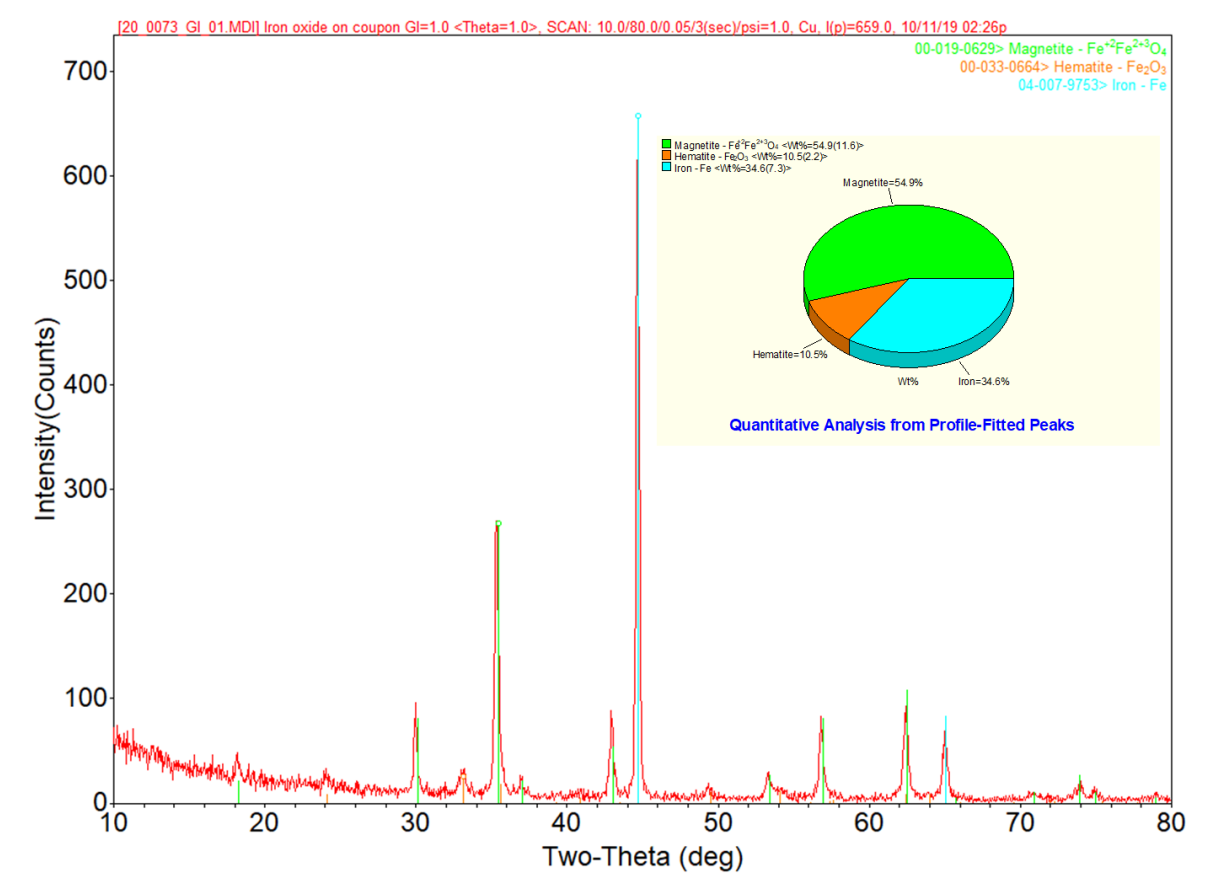

Figure 7. GI-XRD analysis shows three phases: Fe from the substrate, Fe_3O_4 (Magnetite) as the dominant oxide phase, and Fe_2O_3 (Hematite) as an additional oxide phase.

3.3 DFT Results

We consider both ground state BCC α-iron and FCC iron because austenitic steel has the FCC lattice structure. H is more stable in the tetrahedral site than the octahedral site in BCC iron [42,43], and is more stable in the octahedral site in FCC Fe. Using our DFT protocol and the PBE functional, the binding energies of an H atom in these iron structures are 1.99 eV and 2.37 eV, respectively. Using the same PBE functional, the H_2 molecule binding energy is 2.23 eV. At T=0 K, H insertion into BCC Fe is unfavorable by 0.24 eV and favorable in FCC Fe by 0.15 eV. Zero-point energies have not accounted for in these calculations. At finite temperature (both in ambient atmosphere and under high vacuum conditions) H_2 gas concentration is low, which creates a large entropic driving force for H_2 degassing. Experimentally, the hydrogen solubility in various types of steel is on the order of 100 parts per million by weight, which is in qualitative agreement with the above energy estimates [15]. We will use both 1.99 eV and 2.37 eV as references for H atom migration into the oxide.

Inserting an H atom inside a simulation cell that mimics the interior of α-Fe_2O_3 film and optimizing the configuration yields +0.15 eV relative to an H_2 molecule, indicating that it is unfavorable

compared with H inside FCC Fe and favorable compared with H inside BCC. However, zero-point energies (ZPE) have not been accounted for. If we include ZPE=0.5 eV for forming an O-H bond in oxides, and ZPE=0.3 eV in iron metal [43], H insertion from Fe into α-Fe_2O_3 becomes endothermic for both BCC and FCC Fe. In either case, the energy difference between H inside metal and oxide is not large, suggesting that the oxide represents a small thermodynamic hydrogen barrier that can be surmounted even at room temperature as H moves towards the surface. Magnetic moment analysis of Fe_2O_3 simulation cell with a H atom inserted reveals that a Fe(III) is converted to a Fe(II), suggesting that H^+ is formed. During H diffusion in the oxide, the proton motion would be accompanied by electron polaronic motion.

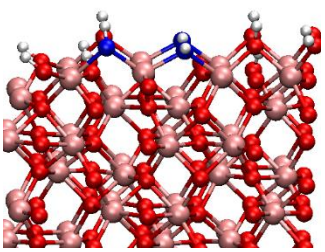

Fig. 8a. Hydroxylated Fe_2O_3 (10-10) surface. Pink, red, and white spheres depict Fe, O, and H atoms. The blue spheres are O on which an extra H atom is added, one at a time.

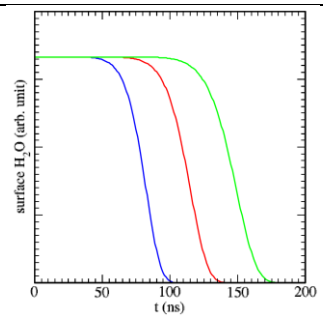

Fig. 8b. Predicted desorption profiles associated with ΔE=0.78 eV (blue), 0.96 eV (red), and 1.15 eV (green), respectively.

On the (0001) oxide surface, the formation of H_2O after adding an H atom is equivalent to adding a H_2O to an O vacancy on that surface. The release of such an H_2O molecule has been predicted to cost more than 1.3 eV [14], and this should be associated with a desorption time scale too slow for Z-applications. Instead, we focus on the hydroxylated (10-10) surface, which contains bridging Fe-(OH)-Fe surface groups [guo2011]. Fig. 8a indicates three surface OH groups on which we add a H atom to mimic H diffusion to the surface, one atom at a time. The energy changes referenced to H inside FCC Fe metal are -0.23 eV, -0.72 eV, and -0.96 eV, respectively. Although there is substantial heterogeneity, the formation of "H_2O" *via* H atom addition is favorable in all cases. The removal of these water molecules to vacuum costs +0.78 eV, +0.96 eV, and +1.15 eV, respectively, after accounting for H_2O energy in vacuum. The cost is significantly less than that on the more stable (0001) surface. We also consider adding two H simultaneously, to two surface OH groups which share a common Fe(III) ion, to investigate whether H will preferentially adsorb on to all possible surface sites before any H_2O comes off. The energy is unfavorable in this case, suggesting that H atoms diffusing from the metal to the surface preferentially land on spatially segregated bridging OH groups.

Next we apply the desorption equation in Ref. [10] to calculate the desorption profile associated with the (10-10) facet. The three water desorption energies computed on the (10-10) surface are adopted as desorption barriers. The kinetic prefactor, kinetic order (one), and temperature dependence of the desorption barrier are taken from Ref. [10]; the cooperative factors are set to zero since water on this surface are found to be segregated from each other; in other words, the desorption energies do not depend on water coverage. The results are depicted in Fig. 8b. Each

curve assumes a population of water with the same desorption activation energy. A temperature (T) ramp is applied such that within 250 ns, T rises from 300 to 1300 K [4,10]. The half-way point of water desorption is found to occur at 80 ns, 112 ns, and 146 ns at the three sites with ascending binding energies (0.78 eV, 0.96 eV, and 1.15 eV) respectively. The instantaneous temperatures at those half-width points are 618 K, 746 K, and 882 K, respectively. These values suggest that desorption of water on the (10-10) surface occurs well within 250 ns Z-shots, and can generate plasma at varying times in the shot.

As water desorbs, O and H are depleted and the Fe(II) content increase at the oxide surface. OH groups can however be replenished *via* hydrogen diffusion from the metal interior. In that sense, the desorption activation energies may continue to change as the Z-shot proceeds, and the kinetic order may deviate from unity as time goes on. This complex kinetics will be considered in future studies.

4. CONCLUSIONS

We synthesized iron oxide films on iron metal surfaces. The experimental analyses of these films show that α-Fe_2O_3 is the dominant oxide phase on the sample and that the surface facets exposed are (0001) and (10-10). DFT calculations of the binding energy of hydrogen on an FCC iron surface, referenced against the binding energy in Fe interior, suggest that the hydrogen prefers to migrate to the surface and remain bound to the (10-10) surface, forming new H_2O molecules. The predicted water desorption energies, fitted to a Temkin-like rate expression, permit water desorption within Z-machine operating conditions and time scales of pulses. On the other hand, water desorption from the (0001) surface associated with water created from this H-reaction route is predicted to be slower. In summary, this report provides a preliminary validation of our hypothesis that hydrogen inside iron domains in steel can react with the surface iron oxide, resulting in formation of water molecules which desorb within Z-machine operating conditions. Further computational work will be conducted to complete this analysis, which will potentially lead to a peer-reviewed publication.

REFERENCES

[1] Thiel, P.A.; Madey, T.E. The Interaction of Water with Solid Surfaces: Fundamental Aspects. *Surf. Sci. Rep.* **1987**, *7*, 211-385.

[2] Revie, R.W. (eds) Uhlig's Corrosion Handbook, Third Edition. (Wiley, 2011)

[3] Cuneo M.E. The Effect of Electrode Contamination, Cleaning and Conditioning on High-Energy Pulsed-Power Device Performance. *IEEE Trans. Dielectr. Electr. Insulation*. **1999**, *6*, 469-485.

[4] Gomez, M.R.; Gilgenbach R.M.; Cuneo M.E.; Jennings C.A.; McBride R.D.; Waisman E.M.; Hutsel B.T.; Stygar W.A.; Rose D.V.; Maron, Y. Experimental Study of Current Loss and Plasma Formation in the Z Machine Post-Hole Convolute. *Phys. Rev. ST Accel. Beams*, **2017**, *20*, 010401.

[5] Bennett, N.; Welch, D.R.; Jennings, C.A.; Yu, E.; Hess, M. H.; Hutsel, B. T.; Laity, G.; Moore, J. K.; Rose, D. V.; Peterson, K.; Cuneo, M.E. Current transport and loss mechanisms in the Z accelerator. *Phys. Rev. ST Accel. Beams*, **2019**, *22*, 0120401.

[6] Yamamoto, S.; Kendelewicz, T.; Newberg, J.T.; Ketteler, G.; Starr, D.E.; Mysak, R.E.; Andersson, K.J.; Ogasawara, H.; Bluhm, H.; Salmeron, M.; Brown, G.E.; Nilsson, A. Water adsorption on α-Fe_2O_3(0001) at near ambient conditions. *J. Phys. Chem. C* **2010**, *114*, 2256-2266.

[7] Nguyen, M.-T.; Seriani, N.; Gebauer, R. Water adsorption and dissociation on α-Fe_2O_3 (0001): PBE+U calculations. *J. Chem. Phys*. **2013**, *138*, 194709.

[8] Schottner, L.; Ovcharenko, R.; Nefedov, A.; Voloshina E.; Wang, Y.; Sauer, J.; Woll, C. Interaction of Water Molecules with the α-Fe_2O_3 (0001) Surface: A Combined Experimental and Computational Study. *J. Phys. Chem. C* **2019**, *123*, 8324-8335

[9] Lane, JMD; Leung, K.; Thompson, A.P.; Cuneo, M.E. Water Desorption from Rapidly-Heated Metal Oxide Surfaces – First Principles, Molecular Dynamics, and the Temkin Isotherm. . *J. Phys. Condens. Matter* **2018**, *30*, 465002.

[10] Leung, K.; Criscenti, L.J.; Robinson, A.C. Quasi-equilibrium Predictions of Water Desorption Kinetics from Rapidly-Heated Metal Oxide Surfaces. *J. Phys. Condens. Matter* **2020**, *32*, 335101.

[11] Guo, H.; Barnard, A.S. Surface structure and environment-dependent hydroxylation of the nonpolar Hematite (100) from Density Functional Theory modeling. *J. Phys. Chem. C* **2011**, *115*, 23023-23029.

[12] Guo, H.; Barnard, A.S. Environmentally dependent stability of low-index hematite surfaces. *J. Coll. Interface Sci.* **2012**, *386*, 315-324.

[13] Ghose, S.K.; Waychunas, G.A.; Trainor, T.P.; Eng, P.J. Hydrated Goethite (α-FeOOH) (100) Interface Structure: Ordered Water and Surface Functional Groups. *Geochim. Cosmochim. Acta* **2010**, *74*, 1943-1953.

[14] Ovcharenko, R.; Voloshina, E.; Sauer, J. Water adsorption and O-defect formation on Fe_2O_3 surfaces. *Phys. Chem. Chem. Phys*. **2016**, *18*, 25560-25568.

[15] Yagodzinskyy, Y.; Todoshchenko, O.; Papula, S.; Hanninen, H. Hydrogen Solubility and Diffusion in Austenitic Stainless Steels Studied with Thermal Desorption Spectroscopy. *Steel Research International* **2011**, *82*, 20-21.

[16] Lee, K.; Yuan, M.; Wilcox, J. Understanding Deviations in Hydrogen Solubility Predictions in Transition Metals through First-Principles Calculations. *J. Phys. Chem. C* **2015**, *119*, 19642-19653.

[17] Ma, L.; Wiame, F.; Maurice, V.; Marcus, P. Origin of Nanoscale Heterogeneity in the Surface Oxide Film Protecting Stainless Steel against Corrosion. *NPJ Materials Degradation* **2019**, *3*, 1332.

[18] Mamede, A.-S.; Nuns, N.; Cristol, A.-L.; Cantrerl, L; Souvi, S.; Cristol, S.; Paul, J.-F. Multitechnique characterization of 304L surface states oxidized at high temperature in steam and air atmospheres. *Appl. Sur. Sci.* **2016**, *369*, 510-519.
[19] Hong, H.; Memom, N.K.; Dong, Z.; Kear, B.H.; Tse, S.D. Flame Synthesis of Gamma-Iron-Oxide (γ-Fe_2O_3) Nanocrystal Films and Carbon Nanotubes on Stainless-Steel Substrates. *Proc. Combustion Institute* **2019**, *37*, 1249-1256.
[20] Allen, G.C.; Harris, S.J.; Jutson, J.A.; Dyke, J.M. A Study of a Number of Mixed Transitional Metal Oxide Spinels Using X-Ray Photoelectron Spectroscopy. *Appl. Sur. Sci*. **1989**, *37*, 111-134.
[21] Henderson, M.A.; Engelhard, M.H. Impact of a mixed oxide's surface composition and structure on its adsorptive properties: case of the $(Fe,Cr)_3O_4(111)$ termination of the α-$(Fe,Cr)_2O_3(0001)$ surface. *J. Phys. Chem. C* **2014**, *118*, 29058-29067.
[22] Yu, X.; Jiang, Z.; Zhao, J.; Wei, D.; Zhou, J.; Zhou, C.; Huang, Q. Local strain analysis of the tertiary oxide scale formed on a hot-rolled steel strip via EBSD. *Surface & Coating Technology* **2015**, *277*, 151-159.
[23] Slattery J.C.; Peng, K.Y.; Gadalla, A.M.; Gadalla, N. Analysis of Iron Oxidation at High Temperatures. *Ind. Engr. Chem. Res*. 1**995**, *34*, 3405-3410.
[24] Chen, C.; Yu, H.; Zheng, S. First-principles study of hydrogen diffusion mechanism in Cr_2O_3. *Sci. China – Tech. Sc.* **2011**, *54*, 88-94.
[25] Zhang, B.; Sun, F.; Zhou, Q.L.; Liao, D.M.; Wang, N.; Xue, L.H.; Li, H.P.; Yan, Y.W. First-principles investigation on stability and mobility of hydrogen in alpha-Al_2O_3 (0001)/alpha-Cr_2O_3 (0001) interface. *Fusion Engr. Design* **2017,** *125*, 577-581.
[26] Li, Q.; Mo, L.-B.; Wang, J.; Yan, K. ; Tang, T.; Rao, Y.-C.; Yao, W.-Q.; Cao, J.-L. Performances of Cr_2O_3-Hydrogen Isotopes Permeation Barriers. *Int. J. Hydrogen Energy* **2017**, *40*, 6459-6464.
[27] Wang, X.; Jiang, M.; Yang, Z. Hydrogen Permeation on Defected a-Al_2O_3 Surfaces: DFT Calculations. **2020**. Cond-mat archive
[28] Kress G. and Hafner J., Ab initio molecular dynamics for liquid metals, Phys Rev B, 47, 1, 1993
[29] Kress G. and Hafner J., Ab initio molecular dynamics simulation of the liquid-metal-amporphous-semiconductor transition in germanium, Phys Rev B, 49, 20, 1994
[30] Kress G. and Furthmuller J., Efficient iterative schemes for ab initio total-energy calculations using plane-wave basis set, Phys Rev B, 54, 16, 1996
[31] Kress G. and Furthmuller J., Efficiency of ab-initio total energy calculations for metals and semiconductors using a plane-wave basis set, Comput. Mat. Sci. 6, 1, 1996
[32] Kohn W. and Sham L. J., Self-Consistent Equations including Exchange and correlation effects, Phys Rev, 140, 1965
[33] Hohenberg P. and Kohn W., Inhomogeneous Electron Gas, Phys. Rev, 136, 38, 1964
[34] Blochl P. E., Projector augmented-wave method, Phys. Rev. B, 50, 24, 1994
[35] Perdew J. P., Burke K., and Ernzerhof M., Genrealized Gradient Approximation made simple, Phys. Rev. Letters, 77, 18, 1996
[36] Monkhorst, H. J. and Pack J. D., Special points for Brillouin-zone integrations, Phys. Rev. B., 13, 12, 1976
[37] Anisimov V. I., Zaanen J., and Andersen O. K., Band theory and Mott insulators: Hubbard U instead of sotner I., Phys. Rev. B., 44, 3, 1991
[38] Anisimov V. I., Solovyev I. V., Korotin M. A., Czyzyk M. T., and Sawatzky G. A., Density-functional theory and NiO photoemission spectra, Phys. Rev. B., 48, 23, 1993

[39] Solovyev I. V. and Dederichs P. H., Corrected atomic limit in the local-density approximation and the electronic structure of d impurities in Rb, Phys. Rev. B., 50, 23, 1994
[40] Maslar J.E., Hurst W.S., Bowers W.J., Hendricks J.H., and Aquino M.I. *In Situ* Raman Spectroscopic Investigation of Aqueous Iron Corrosion at Elevated Temperatures and Pressures. *Journal of The Electrochemical Society*, 147 (7) 2532-2542 (2000)
[41] Marshall C.P., Dufresne W.J.B., and Rufledt C.J. Polarized Raman spectra of hematite and assignment of external modes. *Journal of Raman Spectroscopy*, 1–8 (2020).
[42] Counts, W.A.; Wolverton, C.; Gibala, R. First-Principles Energetics of Hydrogen Traps in a-Fe: Point Defects. *Acta Mater*. **2010**, *58*, 4730-4741.
[43] Sorescu, D.C. First Principles Calculations of the Adsorption and Diffusion of Hydrogen on Fe(100) Surface and in the Bulk. *Catalysis Today* **2005**, *105*, 44-65.

DISTRIBUTION

Email—Internal

Name	Org.	Sandia Email Address
Kyle Cochrane	01641	kccochr@sandia.gov
Anastasia Ilgen	08865	agilgen@sandia.gov
Ronald Goeke	07576	rsgoeke@sandia.gov
Kevin Leung	08865	kleung@sandia.gov
George Laity	01659	grlaity@sandia.gov
Sean Simpson	01656	scsimps@sandia.gov
Allen Robinson	01443	acrobin@sandia.gov
Michael Cuneo	01650	mecuneo@sandia.gov
Matthew Bettencourt	01351	mbetten@sandia.gov
Louise Criscenti	08865	ljcrisce@sandia.lgov
Thomas Gardiner	01641	tagardi@sandia.gov
Mark Rodriguez	01819	marodri@sandia.gov
Technical Library	01911	sanddocs@sandia.gov

Email—External (encrypt for OUO)

Name	Company Email Address	Company Name
Dale Welch	dalew@vosssci.com	Voss Scientific

This page left blank

This page left blank

Sandia National Laboratories is a multimission laboratory managed and operated by National Technology & Engineering Solutions of Sandia LLC, a wholly owned subsidiary of Honeywell International Inc. for the U.S. Department of Energy's National Nuclear Security Administration under contract DE-NA0003525.